

# Model order reduction using hyperreduction methods (DEIM, ECSW) for magnetodynamic FEM problems

Johannes Maierhofer\*, Daniel J. Rixen

Chair of Applied Mechanics, Technical University of Munich, Boltzmannstraße 15, 85748, Garching, Germany

## ARTICLE INFO

### Keywords:

Model-Order-Reduction (MOR)  
Finite-Element-Method (FEM)  
Eddy-current problems  
Magnetodynamic  
Non-linear models  
Energy Conserving Sampling and Weighting (ECSW)  
Discrete Empirical Interpolation Method (DEIM)

## ABSTRACT

Efficient Model Order Reduction Methods for the calculation of non-linear electromagnetic systems can be realized using hyperreduction strategies that are known from structural dynamics. Precalculated full field solution snapshots are used to build a reduction basis using a singular value decomposition. The non-linear behavior is further reduced by a weighting function on selected elements. This paper presents the application of the discrete empirical interpolation method (DEIM) and the energy-conserving sampling and weighting (ECSW) method to magnetodynamic FEM problems. The magnetodynamic FEM formulation is based on the modified vector-potential in combination with edge-elements. Applying the hyperreduction methods, a significant reduction of online computational time was achieved while preserving very good accuracy of the simulation.

## 1. Introduction

The simulation of electrodynamic problems is a common task that is solved using different finite element formulations. Due to Eddy-currents occurring especially in the neighborhood of the boundary of ferro-magnetic domains, a high number of dofs is usually required. To realize an efficient electromagnetic system, the material is often used in its non-linear regime, which significantly increases the computational costs. Especially in the early development phase, Model Order Reduction (MOR) comes in handy to speed up simulations in the design optimization.

Commonly, MOR exploits Proper Orthogonal Decomposition (POD): snapshots of the full order model are used to generate a suitable basis on which the problem can be projected to reduce the number of degrees of freedom. The concept is often used in mechanical systems (see for e.g. [1]) and was shown to be useful also for quasi-static magnetodynamic systems [2,3]. When applied to non-linear problems, the sole projection of the system in a reduced space is not enough to efficiently reduce the computational time since a significant part of the computational cost is not in the solution of linearized problems, but rather in the evaluation of the non-linear contribution of each element to the energy of the problem. This issue has been the focus of recent developments and was investigated for magnetodynamic systems in [4–6] where the DEI-method [7] was applied.

As novel approach of hyperreduction in magnetodynamic systems, the ECSW-method is transferred from structural dynamics to electrodynamic systems as it promises advantages in terms of stability and result quality even for highly reduced models.

This contribution investigates the application and comparison of the discrete empirical interpolation method (DEIM) [7] and the energy-conserving sampling and weighting (ECSW) method [8] to magnetodynamic problems. The systems examined in the course of this work have a few properties that are very specific to magnetodynamic FEM problems and it is not clear how they interfere with hyperreduction methods.

- The problem is strongly in-homogeneous: The solution domain consists of at least two material domains, namely air and a ferro-magnetic material. Their constitutive properties differ up to 3 orders of magnitudes. With that also the field energy distribution is very in-homogeneous.
- The finite element model is built using so-called edge-elements instead of nodal-elements as known from classical structural dynamics.
- Only parts of the system behave dynamically as eddy-currents cannot occur in non-conducting domains as air.

After the theoretical introduction to the used physical equations, the theory of DEIM and ECSW are discussed in a unified notation. A simple 2D example is developed that incorporates all necessary physics

\* Corresponding author.

E-mail addresses: [j.maierhofer@tum.de](mailto:j.maierhofer@tum.de) (J. Maierhofer), [rixen@tum.de](mailto:rixen@tum.de) (D.J. Rixen).

to test and explain the principles of the two hyperreduction methods (DEIM, ECSW) and make a comparison in terms of resulting quality and practical aspects. At the end, a more advanced system in 3D is shown where many more degrees of freedoms are used for the discretization.

## 2. Quasi stationary Maxwell equations

### 2.1. Maxwell equations

The fundamental equations to describe the physics of electrodynamic systems are the Maxwell equations. Oliver Heaviside formulated them in a vector form as

$$\nabla \times \mathbf{E} = -\frac{\partial \mathbf{B}}{\partial t} \quad \text{Faraday's law} \quad (1)$$

$$\nabla \times \mathbf{H} = \mathbf{j} + \frac{\partial \mathbf{D}}{\partial t} \quad \text{Ampere's law} \quad (2)$$

$$\text{div } \mathbf{D} = \rho \quad (3)$$

$$\text{div } \mathbf{B} = 0 \quad (4)$$

	$\mathbf{E}$ :	(V/m)	Electric field
	$\mathbf{D}$ :	(C/m <sup>2</sup> )	Electric flux density
where:	$\mathbf{H}$ :	(A/m)	Magnetic field
	$\mathbf{B}$ :	(kg/s <sup>2</sup> /A)	Magnetic flux density
	$\mathbf{j}$ :	(A)	Current density
	$\rho$ :	(C/m <sup>3</sup> )	Charge density

The response of a material to an external stimulation is described by the constitutive equation. For the governing equations of electromagnetism, there are two constitutive equations. The first is the relation between the electrical field  $\mathbf{E}$  and the electric flux density  $\mathbf{D}$ . Here, the constitutive equation for the electric field is assumed to be linear, isotropic and frequency independent.  $\mathbf{E}$  and  $\mathbf{D}$  are thus related through a constant electrical permittivity  $\epsilon$ .

The second constitutive equation relates the magnetic field  $\mathbf{H}$  and the magnetic flux density  $\mathbf{B}$ . This factor is named magnetic permeability  $\mu$  and is an isotropic, non-linear function of the magnetic field magnitude  $B = |\mathbf{B}|$ . Throughout this work, the magnetic permeability is assumed to be frequency independent. The permeability of a physical material is typically characterized by the relative permeability  $\mu_r$  and the permeability for vacuum  $\mu_0$  which is also called the permeability of free space:

$$\mu(B) = \mu_0 \mu_r(B) \quad (5)$$

$$\mathbf{B} = \mu(B) \mathbf{H} \quad (6)$$

The current density is expressed by the Ohmic law, which accounts for the conductivity  $\sigma$  (isotropic and constant) of the material:

$$\mathbf{j} = \sigma \mathbf{E} \quad (7)$$

### 2.2. Magnetodynamic equations

For magnetodynamic problems, i.e. an approximation of electrodynamic problems with relative low frequency content, the influence of the changing electrical field ( $\frac{\partial \mathbf{E}}{\partial t}$ ) on the magnetic field is neglected in the following. Additionally, it is assumed that, in the whole domain  $\Omega$ , no free charges are present ( $\rho = 0$ ). Assuming that the material does not exhibit any hysteresis, the so-called quasi-stationary Maxwell equations are obtained, which include the effect of Eddy-currents. A more sophisticated derivation can be found in [9]:

$$\nabla \times \mathbf{E} = -\frac{\partial \mathbf{B}}{\partial t} \quad (8)$$

$$\nabla \times \mathbf{H} = \mathbf{j} \quad (9)$$

These partial differential equations, first order in space and time, are valid in a Lipschitz domain  $\Omega \subset \mathbb{R}^2$  or  $\Omega \subset \mathbb{R}^3$ . In Fig. 1, the domains are visualized. In case of an unbounded problem, the domain  $\Omega$  should

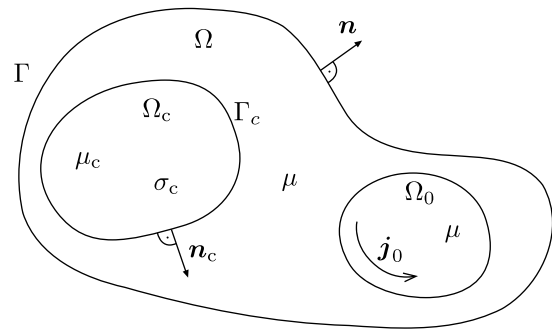


Fig. 1. Domains of the magneto-dynamic equation.

be chosen large enough to properly approximate the propagation of the fields to infinity. The boundary  $\Gamma$  is set such that all field lines have to be tangential to  $\Gamma$ . Eddy-currents only can occur in the electrical conductive domain  $\Omega_c \subset \Omega$  and the conductivity is given by

$$\sigma(\mathbf{x}) = \begin{cases} \sigma_c & \forall \mathbf{x} \in \Omega_c \\ 0 & \forall \mathbf{x} \in \Omega \setminus \Omega_c \end{cases} \quad (10)$$

Because of Eq. (10) and Ohm's law, the Eddy-currents vanish in the domains around  $\Omega_c$  and Eq. (11) must be satisfied [10]:

$$\mathbf{n}_c \cdot \mathbf{j}_c = 0 \quad \text{on } \Gamma_c \quad (11)$$

where  $\mathbf{n}_c$  is the normal to the interface  $\Gamma_c$  and  $\mathbf{j}_c$  denotes the Eddy-currents in  $\Omega_c$ . The excitation current  $\mathbf{j}_0$  is located in domain  $\Omega_0$ , where we assume that no Eddy-currents are present. Therefore, the conductive domains are not overlapping:  $\Omega_0 \cap \Omega_c = \emptyset$ . The full current is  $\mathbf{j} = \mathbf{j}_0 + \mathbf{j}_c$ .

### 2.3. Modified vector potential formulation

The formulation of the problem in terms of the modified vector potential formulation to solve the magnetodynamic equations is generally well-known, although it can be presented in different manners. A very short version is presented here: The vector potential  $\mathbf{A}$  (Vs/m) is defined as

$$\mathbf{B} = \nabla \times \mathbf{A} \quad (12)$$

Substituting Eq. (12) in Faraday's Eq. (8) and Ampere's law Eq. (9) leads to the curl-curl formulation for  $\mathbf{A}$  (see Eq. (14)).

$$\nabla \times \mathbf{E} = -\nabla \times \frac{\partial \mathbf{A}}{\partial t} \quad (13)$$

$$\nabla \times \frac{1}{\mu(B)} \nabla \times \mathbf{A} = \mathbf{j} \quad (14)$$

The gradient of any arbitrary scalar field  $V$  can be added to the vector potential  $\mathbf{A}$  without changing the magnetic field density  $\mathbf{B}$ . Also, a gradient field  $\nabla V$  can be added to the  $\mathbf{E}$ -field. Therefore, considering also the Ohmic Law, Eq. (13) can be used to write the equation expressing the Eddy-current in terms of  $\mathbf{A}$  and  $V$ :

$$\mathbf{j}_c = \sigma \mathbf{E} = -\sigma \frac{\partial \mathbf{A}}{\partial t} + \sigma \nabla V \quad (15)$$

and Eq. (14) can now be written as the governing equation for  $\mathbf{A}$ :

$$\nabla \times \frac{1}{\mu} \nabla \times \mathbf{A} = \mathbf{j}_0 - \sigma \frac{\partial \mathbf{A}}{\partial t} + \sigma \nabla V \quad (16)$$

To find a valid scalar field  $V$ , an additional (naturally given) condition for Eq. (16) is evaluated: The divergence of the right-hand-side (rhs) of Eq. (16) has to be zero as  $\mathbf{H}$  in Eq. (9) can only generate a solenoidal vector field. Additionally, the Coulomb gauging  $\text{div}(\mathbf{A}) = 0$  is applied. With that, the divergence of the first two terms of the rhs of Eq. (16) are zero by default and for the special case of spatially constant conductivity  $\sigma$ , the third term has to satisfy  $\sigma \text{div}(\nabla V) = 0$ .

One valid solution for that is  $V = 0$ , which comes handy, as the degrees of freedom for  $V$  vanish completely [11]. With  $\sigma = 0$  in  $\Omega \setminus \Omega_c$ , the formulation is identical to the magnetostatic formulation. As the vector potential  $\mathbf{A}$  is non unique for the areas of  $\sigma = 0$ , a regularization term is introduced for the system of equations after discretization.

#### 2.4. FEM formulations

Using edge-elements, the problem expressed in terms of modified vector potential can be discretized efficiently [12]. The solution space  $H_A^{\text{curl}}$  for the vector potential is defined as

$$H_A^{\text{curl}}(\Omega) := \{ \mathbf{A} \in [L^2(\Omega)]^3, \nabla \times \mathbf{A} \in [L^2(\Omega)]^3 \} \quad (17)$$

with  $L^2$  being the Hilbert space.

Due to the constant conductivity assumption in the domain  $\Omega_c$  and the use of edge-element, the scalar potential  $V$  does not have to be solved explicitly. The entire problem is described solely by the modified vector potential.

The formulation leads to a weak form: Find  $\mathbf{A} \in H_A^{\text{curl}}$ , such that

$$\begin{aligned} & \int_{\Omega} \frac{1}{\mu} (\nabla \times \mathbf{A}') \cdot (\nabla \times \mathbf{A}) \, d\Omega \\ & + \int_{\Omega_c} \sigma \mathbf{A}' \cdot \frac{\partial \mathbf{A}}{\partial t} \, d\Omega = \int_{\Omega_0} \mathbf{A}' \cdot \mathbf{J}_0 \, d\Omega \end{aligned} \quad (18)$$

for all  $\mathbf{A}' \in H_A^{\text{curl}}$ . A more detailed derivation can be found, e.g. in [13]. To ensure the uniqueness of the vector potential  $\mathbf{A}$  in the area where the conductivity is null, a regularization term  $\epsilon$  is introduced.

$$\int_{\Omega \setminus \Omega_c} \frac{1}{\mu} \epsilon \mathbf{A}' \cdot \mathbf{A} \, d\Omega \quad (19)$$

**Boundary conditions.** The test-function is set to zero on  $\Gamma$ , which is the Dirichlet boundary for  $\mathbf{A}$ . Due to Eq. (12), this means  $\mathbf{n} \cdot \mathbf{B} = 0$ . With that essential boundary, the boundary integral vanishes from the left hand side of the weak form. After discretization, Eq. (20) can be written as

$$\mathbf{M}_A \dot{\mathbf{u}}_A + \mathbf{g}_A(\mathbf{u}_A) = \mathbf{f}_A \quad (20)$$

Hereby  $\mathbf{M}_A$  is the so-called magnetic mass matrix,  $\mathbf{u}_A$  the unknown values of the vector potential,  $\mathbf{f}_A$  the load vector, and  $\mathbf{g}_A$  the discretized internal current. The internal currents are the equivalent to the internal forces known from structural dynamics.

#### 2.5. Mesh

In the area of the skin effect, large gradients for the magnetic field and therefore strong Eddy-current [14] are present. To capture these local effects properly, a fine FE-mesh is required. The element size  $h$  in the area of the skin effect should be small enough to fulfill the condition [13]:

$$\frac{\delta}{h} > 15 \quad (21)$$

Here  $\delta$  is determined by Eq. (22).

$$\delta = \frac{1}{\sqrt{\pi f \sigma \mu}} \quad (22)$$

If the material properties ( $\mu, \sigma$ ) and the frequency range (max frequency  $f$ ) of the simulation are known in advance, Eq. (21) can be taken into account in the mesh generation. Note that the required mesh fineness does not depend on the characteristic size of the problem. This is the driving reason for electro dynamic problems having many degrees of freedom even for simple geometries.

#### 2.6. Transient solver

For systems, operating in the saturated area of the material, the non-linear problem needs to be considered and a simulation of the problem in the time-domain is usually performed.

**Backward Euler algorithm.** The used time integration scheme is the implicit Euler Algorithm (also known as backward Euler Algorithm). It approximates the time derivative by the finite difference

$$\dot{\mathbf{u}}_{n+1} = \frac{\mathbf{u}_{n+1} - \mathbf{u}_n}{\Delta t} \quad (23)$$

where  $\mathbf{u}_n$  and  $\mathbf{u}_{n+1}$  are the solutions at two successive times  $t_n$  and  $t_{n+1}$ ,  $\Delta t$  being the time step  $t_{n+1} - t_n$ .

The problem Eq. (20) can thus be solved at  $t_{n+1}$  as (dropping the subscript  $A$  for simplicity)

$$\mathbf{M} \mathbf{u}_{n+1} + \Delta t \mathbf{g}(\mathbf{u}_{n+1}) = \mathbf{M} \mathbf{u}_n + \Delta t \mathbf{f}_{n+1} \quad (24)$$

which is a non-linear algebraic problem for  $\mathbf{u}_{n+1}$ .

**Newton raphson algorithm.** The non-linear time integration problem Eq. (24) can be written in the residual form

$$\mathbf{r}(\mathbf{u}_{n+1}) = (\mathbf{M} \mathbf{u}_n + \Delta t \mathbf{f}_{n+1}) - (\mathbf{M} \mathbf{u}_{n+1} + \Delta t \mathbf{g}(\mathbf{u}_{n+1})) \stackrel{!}{=} 0 \quad (25)$$

for which the solution can be found by successive linearization

$$\Delta \mathbf{u}_{n+1} = -\mathbf{K}(\mathbf{u}_{n+1}^i)^{-1} \mathbf{r}(\mathbf{u}_{n+1}^i) \quad (26)$$

$$\mathbf{u}_{n+1}^{i+1} = \mathbf{u}_{n+1}^i + \Delta \mathbf{u}_{n+1} \quad (27)$$

where  $\mathbf{K}(\mathbf{u}_{n+1}^i)$  is the tangent stepping matrix of the linearized problem, namely

$$\mathbf{K}(\mathbf{u}_{n+1}^i) = \left. \frac{d\mathbf{r}}{d\mathbf{u}} \right|_{\mathbf{u}_{n+1}^i} = \mathbf{M} + \Delta t \left. \frac{d\mathbf{g}}{d\mathbf{u}} \right|_{\mathbf{u}_{n+1}^i} \quad (28)$$

As stopping condition, an energy-based criterion is chosen. To normalize the criterion value, a reference energy is used. The stopping criterion can therefore be written as:

$$\text{tol} > \left| \frac{\mathbf{r}^T \mathbf{K}^{-1} \mathbf{r}}{\mathbf{f}^T \mathbf{K}^{-1} \mathbf{f}} \right| \approx \left| \frac{\Delta (\mathbf{u}_{n+1}^i)^T \mathbf{r}(\mathbf{u}_{n+1}^i)}{(\mathbf{u}_{n+1}^i)^T \mathbf{f}} \right| \quad (29)$$

### 3. Model order reduction

The need for model order reduction becomes clear by considering the mesh size needed to correctly represent the Eddy-current distribution due to the skin effect. Reduction methods based on projection of the problem in a subspace perform well only for linear problems where the function  $\mathbf{g}(\mathbf{u})$  can be expressed as matrix–vector product that can be projected cost-effectively in a subspace. The focus here is on methods that use a second reduction, the so-called *hyperreduction*, of the non-linear internal forces (i.e. currents for electrodynamic systems) to speed the calculation up. Two methods used in structural mechanics are discussed here. The first approach is called the *Discrete Empirical Interpolation method (DEIM)* and tries to approximate the full non-linear internal forces by expanding the force of selected dofs via a dedicated basis, [7,15]. The second method is the *Energy Conserving Sampling and Weighting Method (ECSW)* that weights selected elements such that the internal forces produce the same virtual work as the non-reduced system, [8]. Both methods gain their time reduction from the idea to reduce the number of elements called for the computation of the non-linear internal force term. A short summary of the methods in the context of structural dynamic systems is given in [16].

**Galerkin projection.** The DEI-Method as well as the ECSW-Method are a combination of a Galerkin projection to a subspace of the solution to reduce the degrees of freedom and a hyperreduction to reduce the non-linear force term to a small evaluation set. To build an appropriate reduction space for the Galerkin projection, the Proper Orthogonal Decomposition (POD) method is often considered. The idea of the POD goes back to the *Karhunen–Loève* theorem around 1950 [17,18], but its broad application grew in the last 20 years with the amount of computational power. The method relies on the Singular Value Decomposition (SVD) which is commonly used today in data science for various purposes to reduce big amounts of data to their characteristic

features [1]. Here, in a pre-processing step, a solution of a representative full problem is computed, while applying an excitation similar to the one applied in further simulations and a SVD of the solution snapshots  $U = [u_1, \dots, u_m]$  is performed. The reduction basis  $V$  contains the most important left singular vectors of that decomposition and the solution is then approximated by

$$u \approx Vq \quad (30)$$

where  $q$  are the generalized degrees of freedom in the reduced space. The reduced problem is then obtained by projection of Eq. (20) on  $V$ :

$$V^T M V \dot{q} + V^T g(Vq) = V^T f \quad (31)$$

#### 4. Discrete empirical interpolation method

The idea of Empirical Interpolation was first proposed in [19] and further developed for discrete problems (DEI-Method) in [7,15]. Its application to structural dynamics problems was investigated in [20,21]. It was applied in combination with a POD to magnetostatic problems in [4,6,22,23]. To preserve the generality of the method's description, the vector  $g(u)$  will continue to be called *internal force* as a generic denomination independent of the underlying physics. For electrodynamic systems the vector describes internal currents.

##### 4.1. Method description

The key idea of DEIM is to find a subspace  $G$  for the internal forces and approximate the full internal force vector  $g(u)$  as linear combination of fewer amplitudes, written in  $c$ . The basis  $G$  is a subspace of the full internal force space, and can thus be used to write the forces as

$$g(u) = Gc(u) + r \quad (32)$$

where  $r$  is a residuum resulting from the approximation in the subspace.

*Internal force subspace.* To build the subspace  $G$  for the internal forces, the internal forces obtained during the pre-processing (representative full simulation) are stored as internal force snapshots  $[g(u_1), \dots, g(u_{n_s})]$ .<sup>1</sup> A representation subspace  $G$  for the internal forces is then generated by performing and truncating a POD on those internal force snapshots.

*Collocation points.* With a truncated  $G$ , equation Eq. (32) is overdetermined. The minimization of  $r$  can be achieved by selecting dofs where Eq. (32) has to be fulfilled:

$$P^T g = P^T Gc \quad (33)$$

The Boolean matrix  $P$  selects the so-called collocation points that are chosen using an empirical greedy algorithm that picks recursively the dof with the biggest residuum of Eq. (32). The internal force can then be approximated as follows, while the superscript + indicates the pseudo inverse:

$$g \approx G(P^T G)^+ P^T g \quad (34)$$

In [21], it is shown that only few DEIM collocation points are needed to represent the nonlinear force vector. Too many collocation dofs could lead to overfitting of the internal force vector and therefore to instabilities in mechanical systems. This effect is not further investigated in this contribution. Further information can be found in [24].

*Evaluated elements.* For this contribution, the number of collocated dofs is chosen to be  $n_s$ . The internal force values at the  $n_s$  chosen collocated dofs needed for the approximation of the full  $g$  have to be evaluated

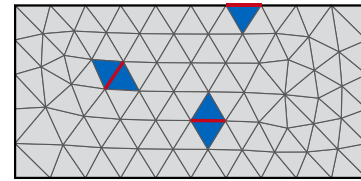


Fig. 2. Generic example of selected DEIM edges and the neighboring elements.

during the solution process. As  $g$  results from a FEM discretization, all neighboring elements have to be evaluated to find the assembled force value at the collocation point. In Fig. 2, the selected dofs in terms of the edge-elements are marked in red. To find the assembled dof value of the internal force, the neighboring elements have to be evaluated.

##### 4.2. Hyperreduction

The whole procedure results in an evaluation of only a subset  $\tilde{\mathcal{E}}$  of elements  $\mathcal{E}$ . This is where the time advantage is achieved. The combination of projections can be precalculated to an auxiliary matrix  $H$ :

$$H = V^T G(P^T G)^+ \quad (35)$$

The hyperreduced internal force vector and tangential stiffness matrix are then given as:

$$g_{r,DEIM}(q) = H P^T \sum_{e \in \tilde{\mathcal{E}}} L_e^T g_e(L_e V q) \quad (36)$$

$$K_{r,DEIM}(q) = H P^T \sum_{e \in \tilde{\mathcal{E}}} L_e^T K_e(L_e V q) L_e V \quad (37)$$

where  $L_e$  is the element localization matrix. Note that, due to the very formulation of DEIM, the reduced tangent matrices are non-symmetric (see Eq. (37)). This can be easily understood if we remember that different basis are chosen for the magnetic potential and the internal forces.

##### 4.3. Different flavors of DEIM

Tiso et al. [20] proposed different variants of DEIM. One important extension is the *unassembled DEIM* (uDEIM). There, the unassembled force vector is calculated and approximated by the projection procedure. The main advantage is the further reduction of evaluated elements. Only one element per DEIM point needs to be processed. For Edge-Elements, this advantage is less significant since less elements are connected over an edge than over a node of an element. Another DEIM extension [25] proposes to generate different local subspaces depending on the current state of the system. The concept is called *localized DEIM* (LDEIM). Using machine-learning techniques the different subspaces are applied dynamically during the simulation which holds the computational effort low by maintaining a high quality result through a wide range of parameters.

#### 5. Energy conserving sampling and weighting method

The concept underlying the ECSW-Method originates from computer graphics and was developed for non-linear finite element dynamic models in mechanical engineering in [8,26] around 2014. The goal is to evaluate only a subset  $\tilde{\mathcal{E}}$  of elements  $\mathcal{E}$  and weigh them with a factor  $\zeta_e > 0$ .

<sup>1</sup> As the internal force snapshots are used to generate a basis for the internal forces, it is also possible to use different solution vectors as those used for the generation of the Galerkin basis  $V$  of the field solution.

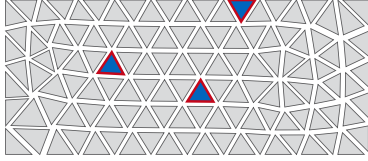


Fig. 3. Generic example of selected ECSW elements and the associated dofs.

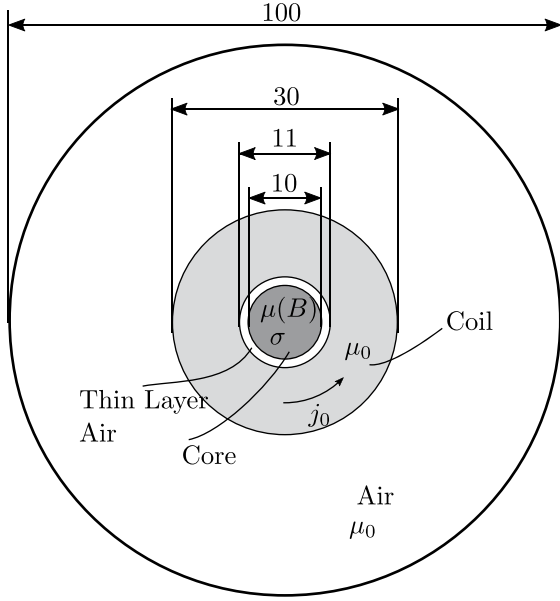


Fig. 4. 2D Geometry (dimensions in millimeter) of the EMPC example.

### 5.1. Method description

The sum over all virtual work contributions, produced in an element by the internal forces, should be approximated as accurately as possible. Therefore, considering the contribution of each element to the reduced force, one can write

$$\begin{aligned} \mathbf{V}^T \mathbf{g}(\mathbf{V}q) &= \sum_{e \in \mathcal{E}} \mathbf{V}^T \mathbf{L}_e^T g_e(\mathbf{L}_e \mathbf{V}q) \\ &\approx \sum_{e \in \tilde{\mathcal{E}}} \zeta_e \mathbf{V}^T \mathbf{L}_e^T g_e(\mathbf{L}_e \mathbf{V}q) = \mathbf{Y} \zeta \end{aligned} \quad (38)$$

where

$$\mathbf{Y} = [\mathbf{V}^T \mathbf{L}_1^T g_1(\mathbf{L}_1 \mathbf{V}q) \dots \mathbf{V}^T \mathbf{L}_\varepsilon^T g_\varepsilon(\mathbf{L}_\varepsilon \mathbf{V}q)]$$

and where  $\zeta$  is only non-zero for the selected set  $\tilde{\mathcal{E}}$ , a subset of the full element set  $\mathcal{E}$ .

**Training sets and sNNLS.** Considering the full solution vectors pre-computed during pre-processing, one can compute the contribution  $\mathbf{V}^T \mathbf{L}_e^T g_e(\mathbf{L}_e \mathbf{V}q_s)$  of each element to the reduced force  $\mathbf{V}^T \mathbf{g}(\mathbf{V}q_s)$  at each computed time step  $t_s$ . This information is then used to find a minimum set of non-zero  $\zeta_e$  to approximate the reduced forces  $\mathbf{V}^T \mathbf{g}(\mathbf{V}q_s)$  up to a given tolerance  $\tau$ . Also, to guarantee the positive definiteness of the associated energy, all weightings in  $\zeta_e$  must be positive. A quasi-optimal set  $\tilde{\mathcal{E}}$  and its associated weights  $\zeta$  can be found by a sparse Non-Negative Least Square (sNNLS) solver. More details on this algorithm can be found in [26].

**Evaluated elements.** As the unassembled forces are used to calculate the virtual work of each element, the weighting factors  $\zeta$  are also at the level of unassembled elements. In Fig. 3 the active elements are marked in blue and their associated dofs in red.

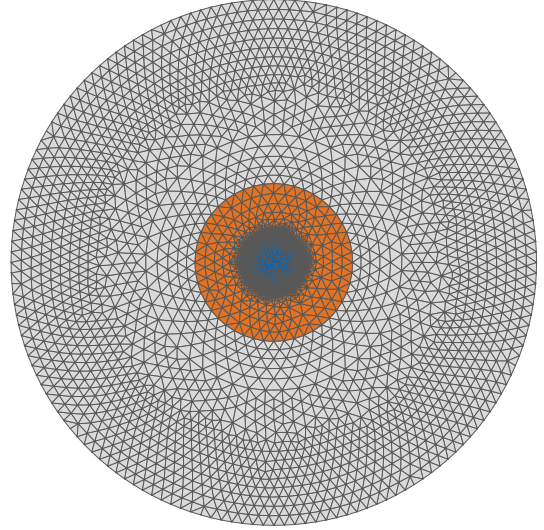


Fig. 5. Triangulated Mesh. The core is marked blue, the coil orange.

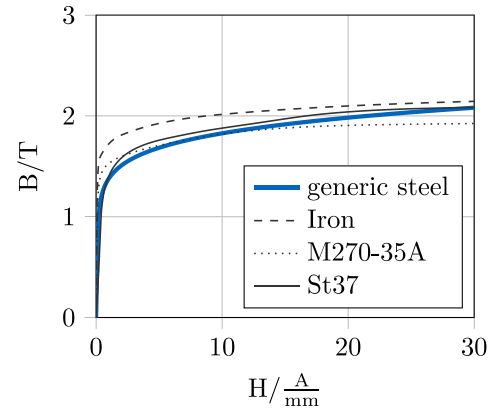


Fig. 6. Material behavior for different types of steel in comparison to the used generic, analytical material law.

### 5.2. Hyperreduction

After finding the reduced set of elements and their associated weighting vector  $\zeta$ , the hyperreduced internal force vector and tangential stiffness matrix are given as:

$$\mathbf{g}_{r,ECSW}(q) = \sum_{e \in \tilde{\mathcal{E}}} \zeta_e \mathbf{V}^T \mathbf{L}_e^T g_e(\mathbf{L}_e \mathbf{V}q) \quad (39)$$

$$\mathbf{K}_{r,ECSW}(q) = \sum_{e \in \tilde{\mathcal{E}}} \zeta_e \mathbf{V}^T \mathbf{L}_e^T \mathbf{K}_e(\mathbf{L}_e \mathbf{V}q) \mathbf{L}_e \mathbf{V} \quad (40)$$

Note here that by construction, the reduced tangent matrix is symmetric and positive definite. This not only reduces the cost in solving the linear problem, but also guarantees stability [26].

### 5.3. Different variants of ECSW

The shown sNNLS is not the only algorithm to find the active set. [27] compares two further mesh sampling algorithms which account for a positive  $\zeta$ , namely the polytope faces pursuit (PFP) solver and the nonnegative variant of the least absolute shrinkage and selection operator (LASSO) [28] which come from the statistics field. In summary, [27] showed that in most of the cases the sNNLS turned out to be the best choice.

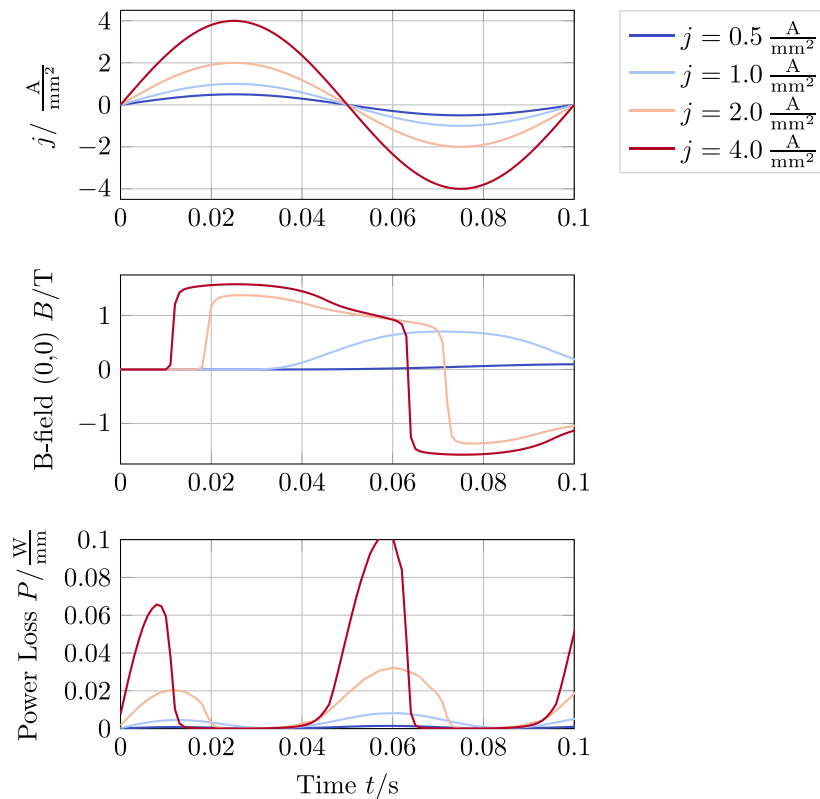
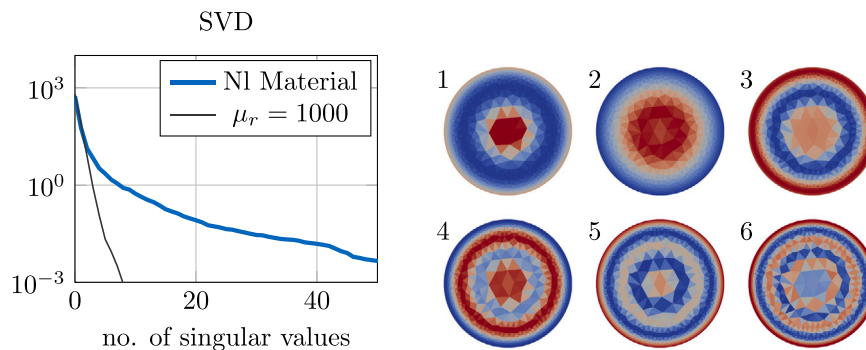


Fig. 7. Reference result for a sine excitation shows strong non-linear behavior in the center of the core.



(a) Singular values for the non-linear material decay slower than for the linear material  $\mu = const.$

(b) First six modes of the basis

Fig. 8. Building the basis from the reference's solution snapshots.

### 6. Example

To illustrate the methods and investigate their applicability, an example denoted here as Electro Magnetic Computing Problem (EMCP) is constructed (Fig. 4). It can be seen as a model for a generic electromagnetic actuator/sensor problem where a solenoid is present. The model is first considered in 2D and will later be extended to 3D.

The system consists of two parts. A cylindrical core of (non-linear) steel is surrounded by a thin layer of air and a concentric coil. The system is embedded in a circular area of air with radius 50 mm. The exciting current density vector  $j$  is considered to be in the transversal cross section (plane perpendicular to the solenoid axis). Therefore, the solution field vector  $A$  will also be in the plane. To achieve a good FEM approximation, edge elements should be taken. So, the finite element discretization is performed in the HCurl-Space, first order with skipping the gradient dofs [29].

**Framework.** All work done for this contribution is performed using the framework *NGSolve* and *Python*. The open source package *NGSolve* is an object oriented finite element core library, written in C++ with a full Python API [30]. Closely connected to it is the automatic mesh generator *NETGEN*, [31] which is capable of meshing 2D and 3D geometries provided by a Constructive Solid Geometry (CSG).

#### 6.1. Reference and training simulation

For the reference simulation, the geometry is meshed with 9502 triangular elements which results in 14331 dofs (Fig. 5). The orange part marks the coil area where the external load  $j$  is applied in a circular manner. The blue part shows the non-linear ferromagnetic material. The rest is modeled as vacuum.

The results of this reference simulation are later used as training data to generate the basis for the solution space and to search for the evaluated elements in the hyperreduction process.

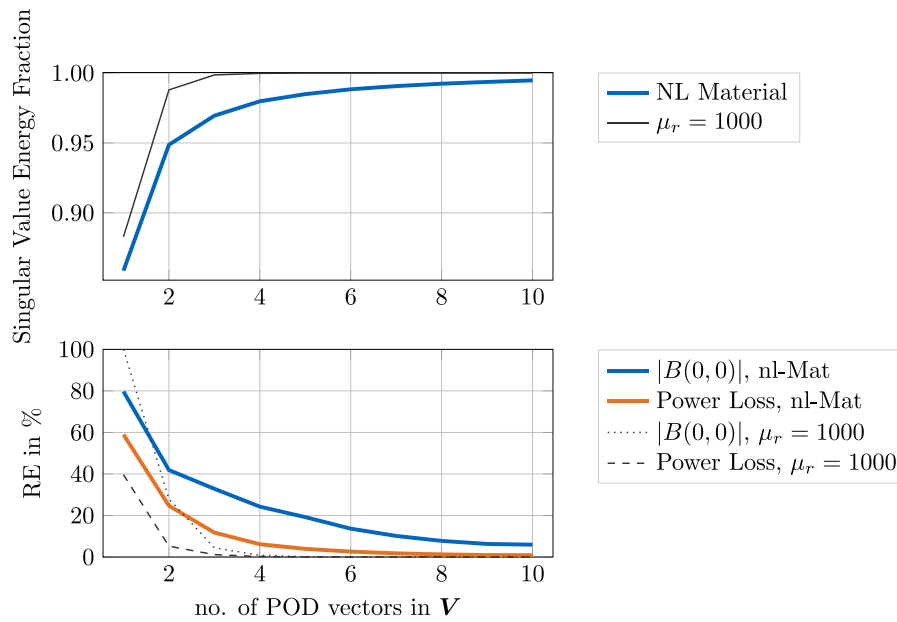


Fig. 9. Relative singular value energy fraction and relative errors of two field quantities as a function of the numbers of basis vectors (2D problem).

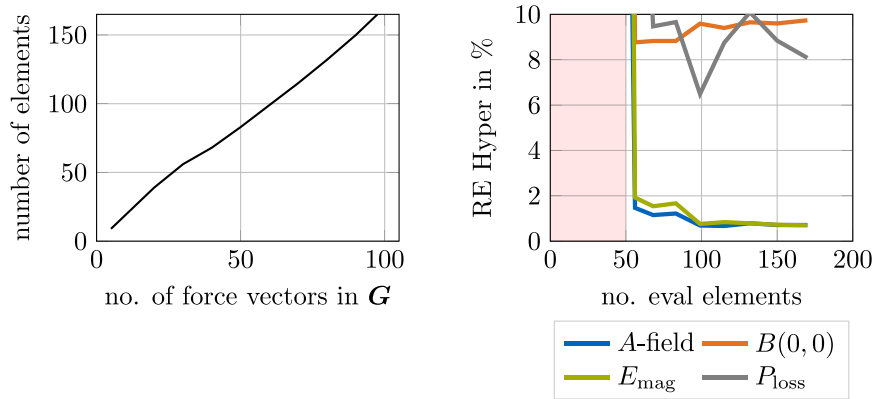


Fig. 10. Relative Error as a function of the number of current modes, comparing the reduced and the hyperreduced solution.

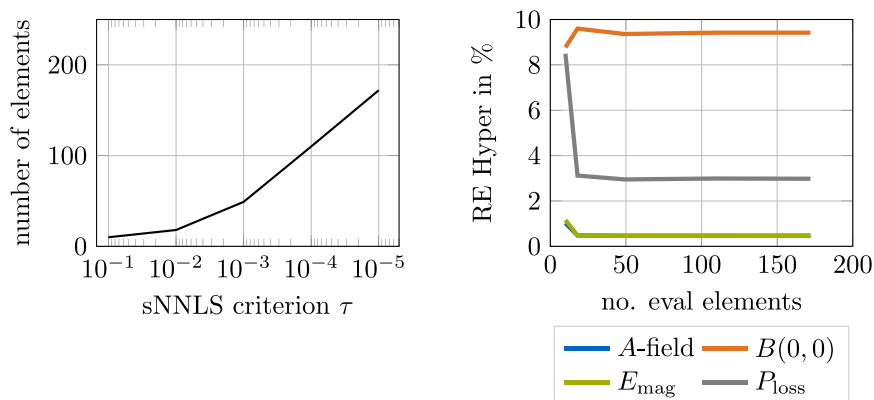


Fig. 11. Number of elements and relative hyperreduction error in dependency of sNNLS tolerance  $\tau$ .

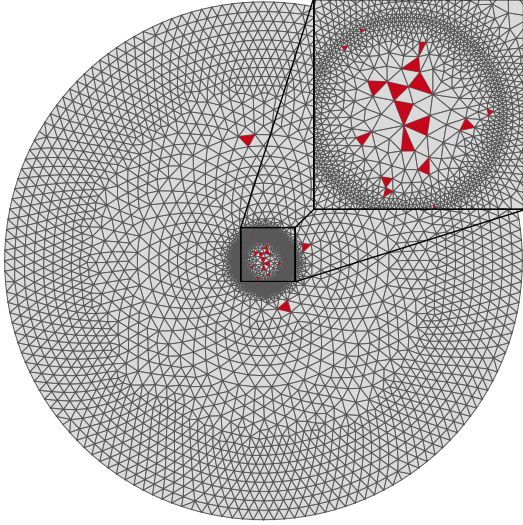


Fig. 12. Selected ECSW elements marked red. Most elements are in the core, only very few in the coil and the air.

**Excitation signal.** The excitation signal for the reference simulation is a current-density (magnitude of  $j$ ) that is applied as a sinus-curve with 10 Hz and an amplitude of  $2 \text{ A mm}^{-2}$ , see Fig. 7. This excitation unveils nicely the non-linear behavior, especially the inertia due to the eddy currents and the saturation of the material.

**Material.** As non-linear material, a generic steel model is proposed. The constitutive equation is formulated as a polynomial such that it is comparable to real interpolated values from material data-sheets (Fig. 6). The expression for the permeability of the material as function of the magnetic flux is formulated as

$$\mu_r(B) = \frac{2000}{0.4 + \left(\frac{B}{T}\right)^8} + 1 \quad (41)$$

where the magnetic flux density  $B$  is given in Tesla (T).

The skin depth where Eddy-currents are dominant is estimated using an averaged  $\mu_r = 1000$  and a conductivity of  $\sigma = 10 \times 10^6 \text{ A V}^{-1} \text{ m}^{-1}$ . From Eq. (21) with an excitation frequency  $f = 10 \text{ Hz}$ , a depth of Eddy-currents of around  $\delta \approx 5 \text{ mm}$  results. The maximum element size is therefore set to  $h = 0.2 \text{ mm}$  in the core mesh.

**Evaluation measures.** The vector field  $A$  is computed for the full problem and, for the discussion, the magnitude of the  $B$ -field is evaluated at the center of the ferro-magnetic material (see Fig. 7). In contrast to this local measure, the magnetic energy Eq. (42) and the power loss Eq. (43) of the system is computed as global measure. The magnetic energy  $W$  and the power loss  $P$  are defined as:

$$W = \int_{\Omega} \int_0^B H(\vec{B}) d\vec{B} d\Omega \quad (42)$$

$$P = \int_{\Omega_c} \frac{|j_c|^2}{\sigma} d\Omega \quad (43)$$

**Timestep.** The time-integration is performed with the backward Euler with a time-step of 0.001 s. Different time-step sizes were tested to verify that the solution is well converged.

**Relative error.** To evaluate the quality of different solutions, a relative error ( $RE$ ) is introduced [26]. This error compares the solution of the reduced problem to the one of the full system over the entire time history of the simulation:

$$RE = \sum_i \frac{\sqrt{\sum_i (\mathbf{u}_{ref}(t_i) - \mathbf{u}(t_i))^T (\mathbf{u}_{ref}(t_i) - \mathbf{u}(t_i))}}{\sqrt{\sum_i \mathbf{u}_{ref}(t_i)^T \mathbf{u}_{ref}(t_i)}} \quad (44)$$

**Discretization convergence.** The convergence of this reference simulation was checked with a second computation of the problem with a mesh having 50% more elements (14 219). The relative error of the evaluation point over all time steps was 0.7%, and the relative error of the power loss was 0.08%. With that, the reference simulation was assumed to be accurate enough for investigating the effect of reduction.

**Computational setup.** The computations were performed on an Intel Xeon CPU E3-1270 v5 @ 3.60 GHz with NGSolve v.6.2.2105 and Python 3.8.12. As linear solver, the SuperLU 5.2.1 direct solver (sparse LU factorization, shipped with Scipy 1.7.1 as *spsolve*) was used. In comparison, also the PARDISO 5 solver via the NGSolve API was tested and found to result in slightly less accuracy but a better performance.

When specifying the number of dofs, only the free dofs are counted, i.e. the dofs that are not restricted by the dirichlet boundary. The dirichlet boundary is applied to the outer boundary of the air volume and set to zero.

**Result.** The reference solution (Fig. 7) exhibits a relatively large phase-lag in the local  $B$ -field at the center of the core due to the damping characteristics arising from the Eddy-currents. Also, the saturation of the material can be seen as the amplitude of the  $B$ -field is limited and does not follow the sinusoidal variation of the excitation. The power loss is the highest when the rate of change of the load is high as then most of the Eddy-currents are induced and converted to heat by the Ohmic resistance. Notice that the system is at rest at the beginning of the simulation. This results in a transient behavior until the system is in a steady state condition. The effect can be seen in the power loss graph.

## 6.2. Basis

To generate the reduction basis, a set of snapshots are decomposed with the SVD algorithm. For this example, all solution vectors of one sinus cycle of the reference problem are considered.

The singular values of the given snapshot matrix are shown in Fig. 8(a) for a linear and the non-linear material. It is obvious that the non-linear system needs more vectors to be approximated in an accurate way. For a better visualization, the rotation of the left singular vectors (dimension of vector potential  $A$ ) of the SV decomposition is taken to represent modes in a magnetic field like structure. Also, only the core is shown in Fig. 8(b). To ensure a good quality of the basis, two different relative errors are calculated with Eq. (44) for the training sets filtered ( $\mathbf{u}_{filtered,n} = \mathbf{V}(\mathbf{V}^T \mathbf{u}_{ref,n})$ ) with the basis  $\mathbf{V}$  constructed from a rising number of POD vectors, shown in Fig. 9. The selected evaluation measures are computed from the filtered solution snapshots. While the error of the power loss in the system is a global measure, the magnitude of the  $B$ -field at the center is a very local measure. This local error is much harder to minimize. To show the difference to a linear system, where very few modes are needed to fully describe the system, the comparison is made for a constant, linear ferro-magnetic material law.

For the further use of the example, the basis is built using the first 8 left singular vectors. They represent 99.2% of the energy. It is a compromise as the error of the local  $B$ -field point is under 10% but it would not decrease much for many more modes.

## 6.3. DEIM - hyperreduction

The subspace for the assembled internal current vector is truncated after the first  $n_S$  left singular vectors. This results in the collocation to  $n_S$  dofs (for the chosen strategy of equal current-modes and collocation dofs), requiring slightly less than  $2n_S$  evaluated elements (boundary dofs do not require two elements).

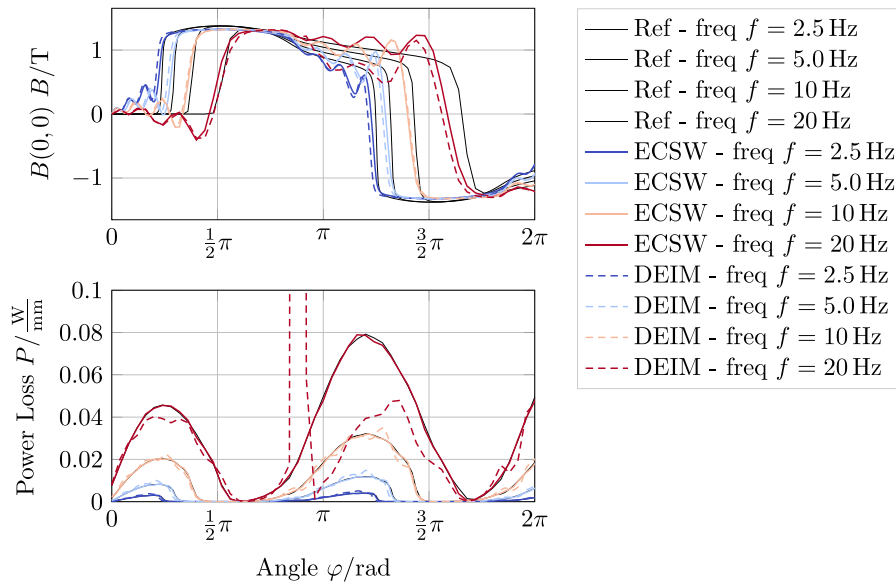


Fig. 13. Comparison of DEIM- and ECSW-model for the variation of excitation frequency with const. amplitude ( $2.0 \text{ A mm}^{-2}$ ).

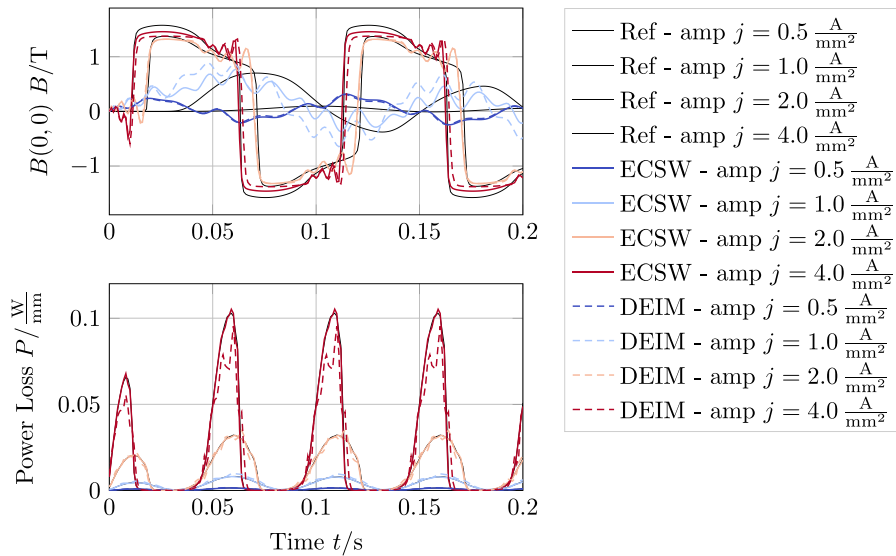


Fig. 14. Comparison of DEIM- and ECSW-model for the variation of excitation amplitude with const. frequency (10 Hz).

**Variation of subspace truncation.** Changing the truncation limit for the current subspace leads to a change of the active elements. The relative error of the vector potential originating from the hyperreduction then decreases (Fig. 10). Interestingly, the decrease is not monotonic and not steep. This can be understood by the fact that the collocation points in DEIM are chosen in a greedy manner and do therefore not guarantee a global optimum.

The relative error depicted in Fig. 10 is relative to the projected solution with the chosen basis. This allows to see the additional error that arises from the hyperreduction. The red marked area shows configurations of the hyperreduced model where the solution is unstable and does not converge. This is definitely a major drawback of the DEIM.

**Solver.** The tangential stepping matrix for the DEIM-reduced model is not symmetric anymore, but is fully populated. Therefore, the solver from LAPACK 3.4 was used via Scipy with the pre-settings for general matrices.

#### 6.4. ECSW - hyperreduction

The 2D problem considered above and hyper-reduced with the DEIM is now considered for hyperreduction with ECSW, using the same reduction basis determined in Section 6.2.

**Variation of  $\tau$ .** To increase the precision of the hyperreduction, the  $\tau$ -criterion of the sNNLS is set to a range from  $1 \times 10^{-1}$  to  $1 \times 10^{-5}$  and plotted in Fig. 11. With decreasing  $\tau$ , the number of active elements rises steadily. However, all the relative error measures of the hyperreduction first increase with decreasing  $\tau$  (which is counter-intuitive), then start falling reaching a plateau. All this in a very small bandwidth of the error. At this place it could not be cleared why the error of the B-field keeps at that plateau and does not improve any more. Obviously, the ECSW Method is always stable and the results are meaningful even for a very low number of evaluated and weighted elements.

The sNNLS with a tolerance of  $\tau = 1 \times 10^{-3}$  selected 49 elements (Fig. 12) with weights in the range from 1.462 to 1991.

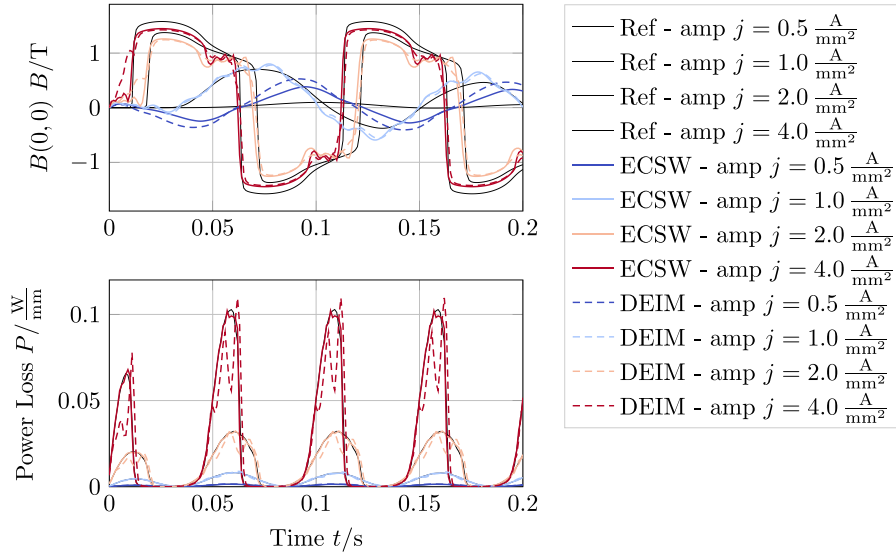


Fig. 15. Comparison of DEIM- and ECSW-model for a training amplitude of  $1.0 \text{ A mm}^{-2}$  for the variation of excitation amplitude with const. frequency (10Hz).

Table 1  
Computational effort values for full- and reduced order model (average values for one time step)

	Full	MOR DEIM	ECSW	rel
Elements	9502	115	110	$\approx 1\%$
Residual Evaluation	0.025 s	0.003 s	0.003 s	$\approx 10\%$
Tangent Matrix	0.056 s	0.001 s	0.001 s	$\approx 2\%$
Dofs	14175	8	$\approx 0.1\%$	
LinSolve	46 ms			
"		0.45 ms		$\approx 1\%$
"			0.08 ms	$\approx 0.2\%$
Iterations	7	5	5	

**Solver.** The reduced linear problem for the ECSW-Method is symmetric and positive definite by nature. Therefore this property can be exploited by the solver. In this case, the non-sparse (the matrix is fully populated), direct Cholesky solver from LAPACK is used via Scipy, due to the additional information that the matrix is positive definite. Note that the SuperLU factorization via Scipy was also tested, but it was always significantly slower. But as seen later, the time for solving the linear problem is only a small portion of the complete computational wall-time.

### 6.5. Evaluation of computational effort

To investigate the computational effort and therefore the achieved speedups for both hyper-reduced models, the solution process is split into three main components. The first step is to apply the latest solution to the non-linear current function to evaluate the residual Eq. (25). Second, the tangential stiffness matrix is built. These two steps correlate with the number of elements. The third step, solving of the linear problem Eq. (26), scales with the number of dofs the projected system results in. Table 1 shows the results, separated by a horizontal line for the element number dependent sizes and the dof number dependent ones. All steps are iterated until the convergence is reached. All computational times are given for one simulation time-step, meaning that the computational times for every iteration are summed up during the convergence of one time step. As the number of iterations will vary due to the actual load- and system state, all times are averaged over the whole trajectory (i.e. all time steps) of the simulation. It should be noted here that no outliers regarding the times could be identified.

There is a limit to the achievable time reduction due to some overhead time for data-handling operations which becomes obvious in the step of the residual evaluation. A slight drawback of the DEIM hyperreduction can be seen in the fact that the reduced matrix is not symmetric and therefore needs a more advanced solver which takes a bit more time. In the further course of the paper, computational time data are omitted, since they correlate mainly with the element number as shown here whatever hyperreduction method is used.

For the next test, the number of current vectors in DEIM and the tolerance  $\tau$  for approximating (Eq. (38)) are tuned to keep roughly the same number of elements. So we will compare the results in terms of accuracy, the number of elements evaluated in the hyperreduction (and thus the computational time) being similar.

### 6.6. Methods comparison — test trajectory

The obtained hyperreduction parameters (Basis  $V$ , DEIM: active elements and current-basis  $G$ , ECSW: active elements and weighting vector  $\zeta$ ) are now frozen and stored for the next reduced computation. Both reduction methods are constructed such that they evaluate approximately the same amount of elements (Table 2). With that, the time savings are roughly the same, but the quality of the results is examined. First, the stored reduced models are excited with a different frequency applied. As far as the mesh density is high enough to represent the correct eddy currents (see Eq. (22)), the reduced models should be quite independent on the frequency thus the reduced results are close to the reference. The results in Fig. 13 are plotted over one period of four different frequencies, where 10 Hz was the training excitation. The ripples arise from the low number of used modes in the Galerkin projection. Both methods show a very similar behavior, except one point where the DEIM-method has an unstable point in the power loss while the ECSW always produces smooth results.

Second, the frequency is kept at the training frequency (10 Hz) and the amplitude of the excitation is varied. For a training amplitude of  $2 \text{ A mm}^{-2}$ , Fig. 14 unveils the weak representation of low amplitude behavior for the local probe point. For the global measures the ECSW-method outperforms the DEIM-method clearly as the results are much smoother and very close to the reference solution.

As seen in Fig. 14, the reduced models only behave well in the near of the trained amplitudes. Performing the same experiment but with a training amplitude of  $1.0 \text{ A mm}^{-2}$  leads to Fig. 15. This leads to a better representation of the local measures and does not effect the high load

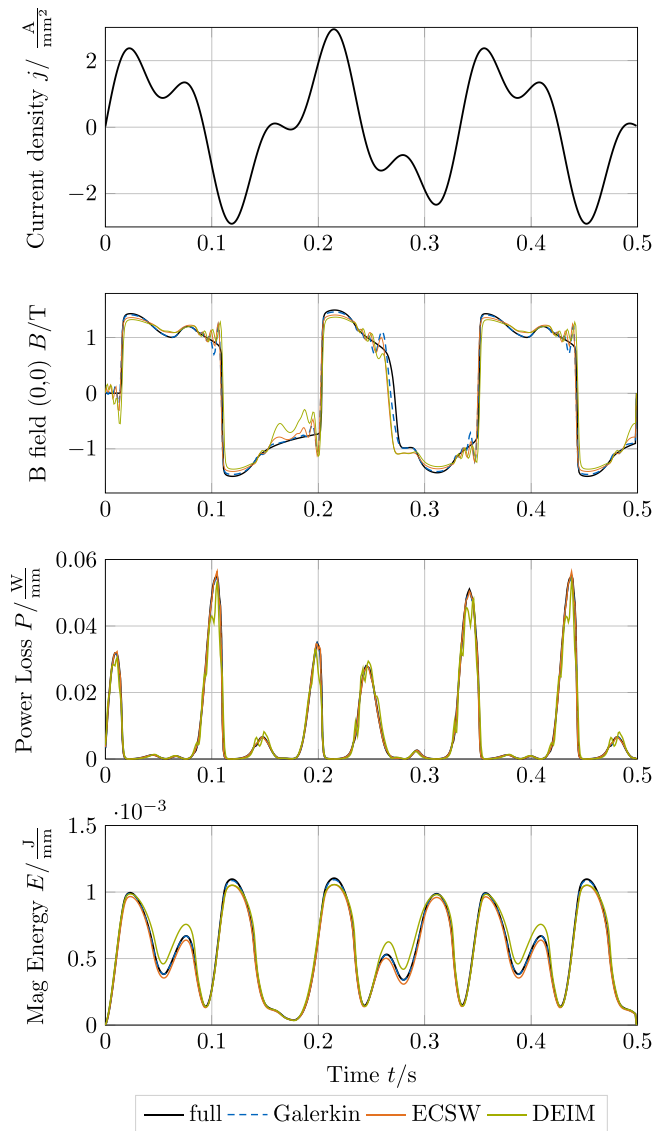


Fig. 16. Reference result for an arbitrary test trajectory. Galerkin  $n = 8$ , ECSW  $\tau = 1 \times 10^{-3}$ , DEIM  $n_f = 30$ .

performance too much. The advantage of the ECSW-method for global measures becomes even more evident.

To further test and compare these stored reduced models, a new current excitation consisting of two superimposed sinus Eq. (45) is applied to the system.

$$f(t) = 2 \cdot \sin(6 \text{ Hz} \cdot t) + 1 \cdot \sin(15 \text{ Hz} \cdot t) \quad (45)$$

Simulations are then run for the full system, pure Galerkin projection (reduction without hyperreduction), and DEIM and ECSW hyperreduction (training: 10 Hz,  $2.0 \text{ A mm}^{-2}$ ) methods (Fig. 16) with a timestep 0.001 s and 500 steps.

In Fig. 16, one observes that the hyperreduced solution is qualitatively accurate but adds additional errors of the order of the error inherent to the projection of the reduction basis itself (i.e. the Galerkin projection is done without hyperreduction). Qualitatively, the DEIM shows spurious peaks in the power loss, for example at  $t \approx 0.25$  s. This could eventually be reduced by changing the number of collocation points.

The relative errors are computed with the full simulation as reference and listed in Table 2. It must be highlighted that the global relative

Table 2

Comparison of DEIM and ECSW results using the relative error of the vector potential field.

Reduction	dofs	elements	$RE_{A\text{-field}}$	$RE_{Mag\text{Energy}}$	$RE_{B_{(0,0)}}$
Full	14175	9502	–	–	–
POD	8	9502	0.25 %	0.5 %	8.6 %
POD + DEIM	8	56	3.1 %	5.2 %	14 %
POD + ECSW	8	49	0.84 %	1.85 %	13 %

Table 3

Training parameters for the 3D example study.

Parameter	Value
Excitation	sine, 10 Hz
Amplitude	$6 \text{ A mm}^{-2}$
$\Delta t$	0.001 s
Timesteps	100

error measures are clearly better using the ECSW-Method even though less elements evaluated.

**Outcome.** Both methods result in a similar behavior in the representation of the local field for load cases similar to the training sets, while the result’s quality is quite independent of the load’s frequency. To improve the overall local accuracy, a better basis would be needed.

From a global point of view, the ECSW-result can be considered as better: although a few less elements than for the DEIM where considered, all the relative error measures are smaller, as can be seen from Table 2. Also qualitatively, the ECSW never introduced spurious peaks and estimated the power loss very precisely. The ECSW method seems to rather underestimate the magnetic energy in the system and is overall closer to the full simulation. This is confirmed by the relative error of the magnetic energy.

## 7. Advanced example

To further investigate the performance of the methods, a more complex example is shown here. It is based on the same problem shown before but now is in 3D. Also, a mobile target part is now included and modeled as ferro-magnetic material (Fig. 17(a)). Again the number of current-modes in DEIM and the criterion  $\tau$  in ECSW are chosen to roughly evaluate the same amount of elements. The problem parameters are listed in Table 3.

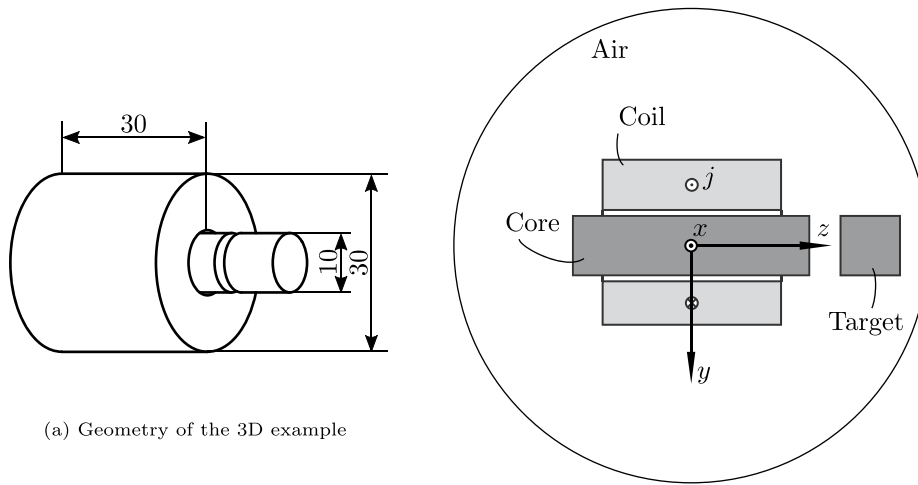
The geometry is embedded in a sphere of air with 50 mm radius. Meshing results in a system with 33910 elements and 40159 total dofs.

### 7.1. Training simulation

To find the active elements for the hyperreduction, again the simple sine trajectory is computed full order for one period as training simulation and analyzed as shown before. It needs to be mentioned here that the current density is not directly comparable between the two examples. In the previous example, the cross section of the coil is in the transverse plane, whereas in this example the cross section to calculate the load is in the sagittal plane. With the knowledge of the previous test, the training set should not cause a high saturation result to enable a wide amplitude tolerance in the reduced model (see Figs. 18 and 19).

Because of the smoother training results with the less pronounced non-linearity, the axis-symmetric system is very well described by 8 modes.

Evaluating the offline time that is needed to select the active elements that have to be computed later, two things stand out from Table 4. First, the selection via DEIM does rarely scale with the number of chosen current modes. For small numbers this is rather malicious but for higher number of elements this becomes a benefit. The sNNLS for



(a) Geometry of the 3D example

(b) Cross section of the System (not drawn to scale)

Fig. 17. 3D Example system.

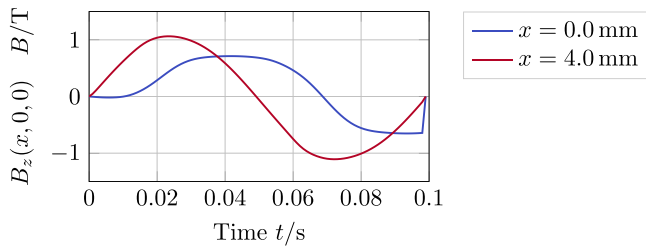


Fig. 18. Reference result in the core for two different radial positions: Center  $x = 0$ , near boundary  $x = 4.0$  mm. The non-linearity is not very pronounced in the training snapshots.

Table 4

Number of chosen elements and wall-times for the offline calculations of the DEI- and ECSW-Methods from the training snapshots for different strength of hyperreduction.

	Parameter	Duration	Active Elements
DEI	$n_S = 2$	21 s	13
	$n_S = 5$	21 s	28
	$n_S = 10$	21 s	53
sNNLS	$\tau = 1 \times 10^{-2}$	1.7 s	9
	$\tau = 1 \times 10^{-3}$	4.9 s	20
	$\tau = 1 \times 10^{-4}$	19 s	52

Table 5

Computational wall-times in the solution process of the 3D training simulation.

	Full	MOR	Rel
Elements	33910	20	$\approx 0.05\%$
Residual Evaluation	0.33 s	0.015 s	$\approx 5\%$
Tangent Matrix	0.84 s	0.002 s	$\approx 0.2\%$
Dofs	39169	8	$\approx 0.02\%$
Iterations	3	3	
LinSolve (SuperLU)	40 s	0.0002 s	$\approx 5 \times 10^{-4}\%$
LinSolve (PARDISO)	2 s	0.0002 s	$\approx 0.01\%$

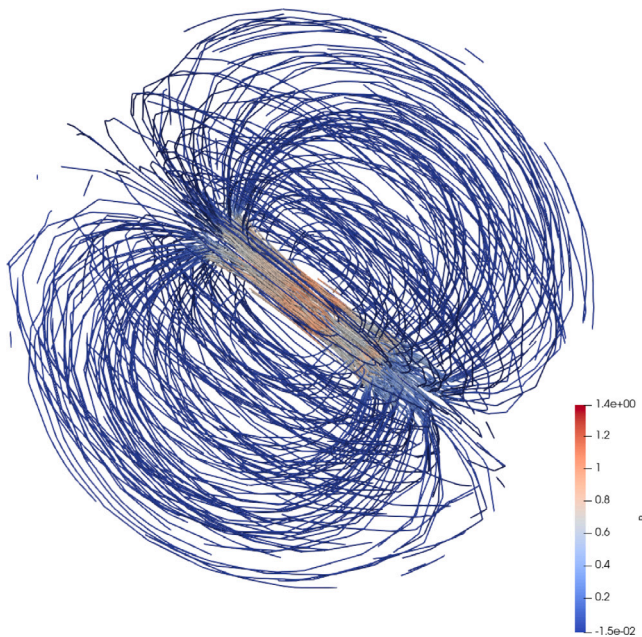


Fig. 19. Field lines of B-field.

the ECSW-Method scales directly with the tightness of the tolerance  $\tau$ . For too strong demands, the algorithm will even fail and does not converge. From that perspective, the DEIM is more robust.

*Onboard validation — speedups.* To discuss the gained speedup of the hyperreduction methods, one exemplary ECSW simulation with the same load trajectory (sine) as the training setup was chosen. The main solution process parts are then evaluated as shown in the 2D section. The computational time does not only scale directly with the number of evaluated elements. That is because of some programming overhead that keeps constant for every Newton-iteration. This can be further improved, in which case the advantages of calculating only a fraction the elements would become even more apparent. The bottleneck of this computation is (see Table 5) obviously the evaluation of the residuum which is performed in every Newton-Iteration. The savings in the solution process itself seem very high. By using the PARDISO-Solver which is much more optimized, this point is somewhat put into perspective.

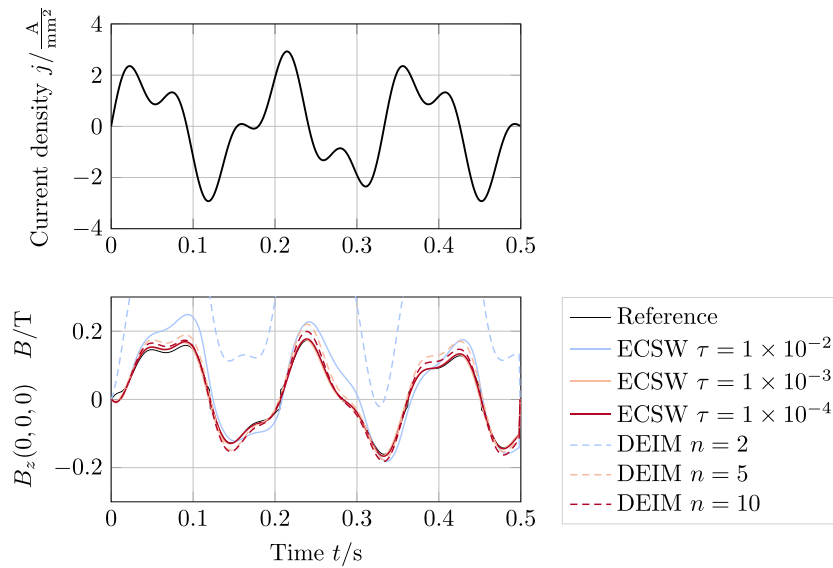


Fig. 20. Low excitation result. The smallest DEI-model cannot represent the local field.

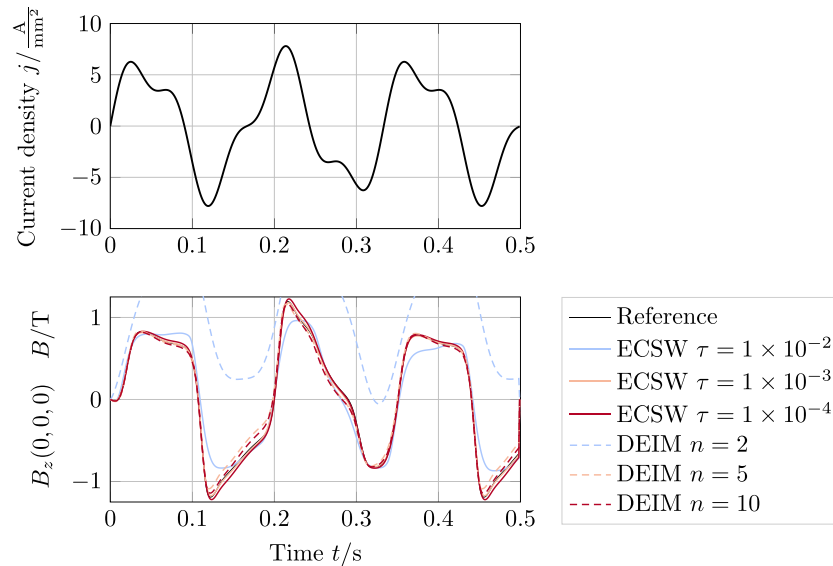


Fig. 21. Medium excitation result. Again the smallest DEI-model is not capable of reproducing the local B-field values.

7.2. Result for test trajectory

To test the reduced model, again a unknown test trajectory is applied to the reduced model and validated against a full order reference simulation. The results are shown in Table 6. The full order model needs already wall times of around 20h with the SuperLU-Solver or 1.25h using the PARDISO-Solver.

Three different load cases are applied to the reduced models which differ mainly in their amplitude (low  $\approx 2 \text{ A mm}^{-2}$ , medium  $\approx 6 \text{ A mm}^{-2}$ , high  $\approx 8 \text{ A mm}^{-2}$ ). The reduced models differ in their number of elements as seen in Table 4.

In Figs. 20, 21, 22, the reduced model results are plotted for the 3 sets of reduction parameters. The plots for the power loss and the magnetic field energy are not shown here, as they do not differ in any method in a visible way. It is noticeable that the approximation with only 2 current modes is very wrong and cannot represent the dynamics in any way. The result becomes much better when taking into account 5 current modes. Interestingly, the curve seems to run away for

longer simulation time. This needs to be further evaluated. The ECSW-method performs very predictable even when taking only 5 elements, the result is close to the reference. By tightening of the tolerance  $\tau$ , the quality of the result increases to nearly perfect representation of the system's dynamic. Also here, the ECSW-Method is more reliable as it keeps the result bounded close to the true reference. The wall-time for the reduced model is around 6min to 9min without further code optimization. This represents a significant saving compared to the full solution (1.25h).

From Table 6, one can draw the preliminary conclusion that the ECSW-Method performs superior DEIM in terms of result quality in relation to the number of evaluated elements. It is clearly noticeable that the ECSW-Method is more predictable as for more elements the relative error steadily decreases. The DEIM in contrast shows weakness for higher amplitudes as trained. Increasing the number of elements can even worsen the result.

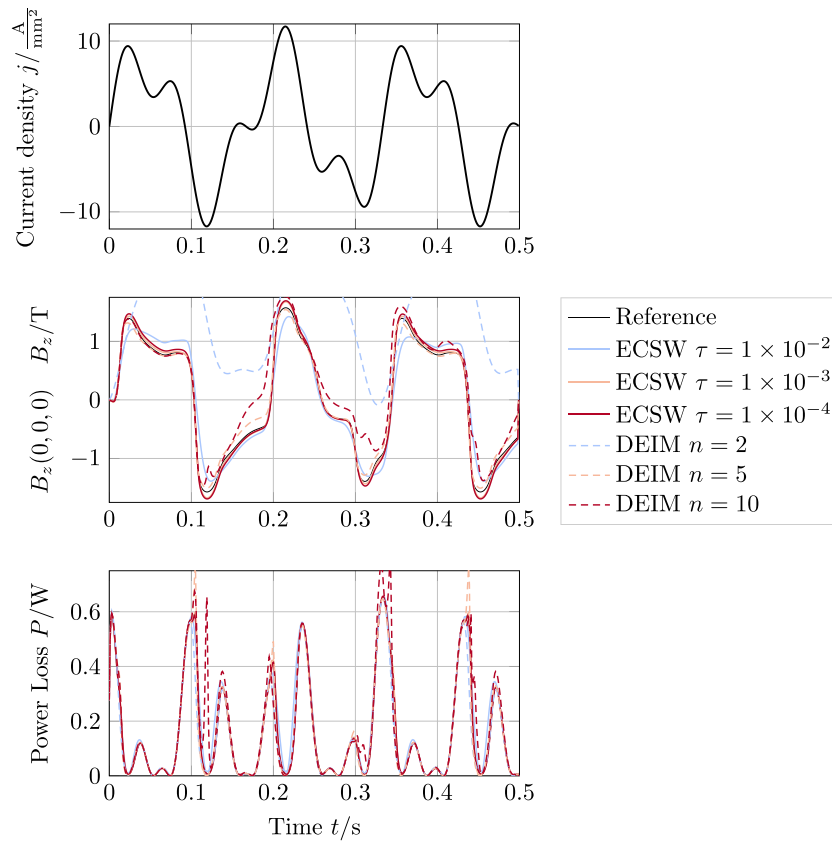


Fig. 22. High excitation results. Even the higher order DEI-models cannot represent the local B-field values well and additionally show spurious peaks in the power loss.

Table 6

Relative Errors of the global power loss of the 3D example for different parameters and excitations for each of the two hyperreduction methods over all 500 timesteps.

Reduction	dofs	elements	Low	Medium	High
			$RE_{P_{loss}}$	$RE_{P_{loss}}$	$RE_{P_{loss}}$
Full	39169	33910	–	–	–
POD	8	33910	0.08 %	0.42 %	0.63 %
POD + DEIM	8	13	2.51 %	8.6 %	16.56 %
POD + DEIM	8	28	0.58 %	3.55 %	10.24 %
POD + DEIM	8	53	0.34 %	2.44 %	27.65 %
POD + ECSW	8	9	0.6 %	5.28 %	14.11 %
POD + ECSW	8	20	0.16 %	0.61 %	2.73 %
POD + ECSW	8	52	0.10 %	0.33 %	1.35 %

## 8. Summary & conclusion

### 8.1. Methods comparison

Both, the DEI- and the ECSW-methods use information of the internal currents. For the DEIM, a basis is extracted which is then used for a collocation based interpolation. ECSW uses them for the calibration of weighting factors of a quadrature of the energy. For the shown generic example of a solenoidal system, computational speed-ups of up to one order of magnitude were achieved. Although care was taken to implement all methods properly in the framework of NGSolve, a further significant reduction of computational time could be achieved by putting additional effort in code optimization. In these examples, the resulting accuracy of the applied ECSW method is better than the DEIM for a similar number of elements kept in the hyperreduction. Comparing the 2D with the 3D example shows that, for bigger systems, it is easier to gain a higher speed-up while still preserving a very high accuracy.

### 8.2. Closing

Concluding, both shown hyperreduction methods have potential to reduce electro-dynamic systems drastically. Finding a good reduction basis is identified as key to a successful reduction. The hyperreduction part is found to be quite robust and does not degrade the result markedly but is essential to significantly reduce the computational costs of the reduced model. While the DEIM has the major disadvantage that it can lead to unstable models, the ECSW-Method exhibits high robustness and better results for less evaluated elements. The next step to raise the full potential of the ECSW method is to introduce a geometry parameter and solve the reduced system without new reduction for neighboring configurations. For that purpose the target body of the shown example will become a mobile target in  $z$ - and  $y$ -direction. Future work will include more advanced geometries with less symmetry. Also the generation of the projection basis using less training snapshots is part of the investigation.

### Declaration of competing interest

The authors declare that they have no known competing financial interests or personal relationships that could have appeared to influence the work reported in this paper.

### References

- [1] Gaetan Kerschen, Jean Claude Golinval, Alexander F. Vakakis, Lawrence A. Bergman, The method of proper orthogonal decomposition for dynamical characterization and order reduction of mechanical systems: An overview, *Nonlinear Dyn.* 41 (1-3) (2005) 147–169, <http://dx.doi.org/10.1007/s11071-005-2803-2>.
- [2] Daniel Schmidthausler, Markus Clemens, Low-order electroquasistatic field simulations based on proper orthogonal decomposition, *IEEE Trans. Magn.* 48 (2) (2012) 567–570, <http://dx.doi.org/10.1109/tmag.2011.2174042>.

- [3] Yuki Sato, Hajime Igarashi, Model reduction of three-dimensional eddy current problems based on the method of snapshots, *IEEE Trans. Magn.* 49 (5) (2013) 1697–1700, <http://dx.doi.org/10.1109/tmag.2013.2241412>.
- [4] Thomas Henneron, Stephane Clenet, Model order reduction of non-linear magnetostatic problems based on POD and DEI methods, *IEEE Trans. Magn.* 50 (2) (2014) 1–4, <http://dx.doi.org/10.1109/TMAG.2013.2283141>.
- [5] Thomas Henneron, Stephane Clenet, Model-order reduction of multiple-input non-linear systems based on POD and DEI methods, *IEEE Trans. Magn.* 51 (3) (2015) 1–4, <http://dx.doi.org/10.1109/tmag.2014.2347416>.
- [6] Yuki Sato, Markus Clemens, Hajime Igarashi, Adaptive subdomain model order reduction with discrete empirical interpolation method for nonlinear magneto-quasi-static problems, *IEEE Trans. Magn.* 52 (3) (2016) 1–4, <http://dx.doi.org/10.1109/tmag.2015.2489264>.
- [7] Saifon Chaturantabut, Danny C. Sorensen, Nonlinear model reduction via discrete empirical interpolation, *SIAM J. Sci. Comput.* 32 (5) (2010) 2737–2764, <http://dx.doi.org/10.1137/090766498>.
- [8] Charbel Farhat, Todd Chapman, Philip Avery, Structure-preserving, stability, and accuracy properties of the energy-conserving sampling and weighting method for the hyper reduction of nonlinear finite element dynamic models, *Int. J. Numer. Methods Eng.* 102 (5) (2015) 1077–1110, <http://dx.doi.org/10.1002/nme.4820>.
- [9] Manfred Kaltenbacher, Numerical simulation of mechatronic sensors and actuators, *Numerical Simulation of Mechatronic Sensors and Actuators*, 2007, pp. 1–428, <http://dx.doi.org/10.1007/978-3-540-71360-9>.
- [10] Arnulf Kost, *Numerische Methoden in der Berechnung elektromagnetischer Felder*, Springer, 1994, <http://dx.doi.org/10.1007/978-3-642-57910-3>.
- [11] O. Biro, K. Preis, On the use of the magnetic vector potential in the finite-element analysis of three-dimensional eddy currents, *IEEE Trans. Magn.* 25 (4) (1989) 3145–3159, <http://dx.doi.org/10.1109/20.34388>.
- [12] A. Kameari, Three-dimensional eddy current calculation using finite element method with A-V in conductor and omega in vacuum, *IEEE Trans. Magn.* 24 (1) (1988) 118–121, <http://dx.doi.org/10.1109/20.43870>.
- [13] Gérard Meunier, *The finite element method for electromagnetic modeling*, vol. 33, John Wiley & Sons, 2010, <http://dx.doi.org/10.1002/9780470611173>.
- [14] Patrick Dular, Ruth V. Sabariego, Johan Gyselinck, Laurent Krähenbühl, Subdomain finite element method for efficiently considering strong skin and proximity effects, *COMPEL-Int. J. Comput. Math. Electr. Electron. Eng.* 26 (4) (2007) 974–985, <http://dx.doi.org/10.1108/03321640710756311>.
- [15] Paolo Tiso, Daniel J. Rixen, Discrete empirical interpolation method for finite element structural dynamics, in: *Topics in Nonlinear Dynamics*, Volume 1, Springer New York, 2013, pp. 203–212, [http://dx.doi.org/10.1007/978-1-4614-6570-6\\_18](http://dx.doi.org/10.1007/978-1-4614-6570-6_18).
- [16] Matthew S. Allen, Daniel Rixen, Maarten van der Seijs, Paolo Tiso, Thomas Abrahamsson, Randall L. Mayes, *Substructuring in Engineering Dynamics*, Springer International Publishing, 2020, <http://dx.doi.org/10.1007/978-3-030-25532-9>.
- [17] K. Karhunen, Über lineare methoden in der wahrscheinlichkeitsrechnung, *Annals of Academic Science Fennicae, Series A1 Mathematics and Physics* 37 (1946).
- [18] M. Loève, *Fonctions Aléatoires du Second Ordre, Processus stochastiques et mouvement Brownien* (1948).
- [19] Maxime Barrault, Yvon Maday, Ngoc Cuong Nguyen, Anthony T. Patera, An ‘empirical interpolation’ method: application to efficient reduced-basis discretization of partial differential equations, *Comptes Rendus Mathématique* 339 (9) (2004) 667–672, <http://dx.doi.org/10.1016/j.crma.2004.08.006>.
- [20] Paolo Tiso, Rob Dedden, Daniel Rixen, A modified discrete empirical interpolation method for reducing non-linear structural finite element models, in: *Volume 7B: 9th International Conference on Multibody Systems, Nonlinear Dynamics, and Control*, American Society of Mechanical Engineers, 2013, <http://dx.doi.org/10.1115/DETC2013-13280>.
- [21] Annika Radermacher, Stefanie Reese, Pod-based model reduction with empirical interpolation applied to nonlinear elasticity, *Int. J. Numer. Methods Eng.* 107 (6) (2015) 477–495, <http://dx.doi.org/10.1002/nme.5177>.
- [22] M. Al Eit, F. Bouillault, C. Marchand, G. Krebs, Model-order nonlinear subspace reduction of electric machines by means of POD and DEI methods for copper losses calculation, in: *International Journal of Numerical Modelling: Electronic Networks, Devices and Fields*, 31, (2) 2018, <http://dx.doi.org/10.1002/jnm.2274>.
- [23] Fabian Muller, Andreas Siokos, Johann Kolb, Martin Nell, Kay Hameyer, Efficient estimation of electrical machine behavior by model order reduction, *IEEE Trans. Magn.* 57 (6) (2021) 1–4, <http://dx.doi.org/10.1109/tmag.2021.3070183>.
- [24] MD. Rokibul Hasan, Laurent Montier, Thomas Henneron, Ruth V. Sabariego, Stabilized reduced-order model of a non-linear eddy current problem by a gappy-POD approach, *IEEE Trans. Magn.* 54 (12) (2018) 1–8, <http://dx.doi.org/10.1109/tmag.2018.2866449>.
- [25] Benjamin Peherstorfer, Daniel Butnaru, Karen Willcox, Hans-Joachim Bungartz, Localized discrete empirical interpolation method, *SIAM J. Sci. Comput.* 36 (1) (2014) A168–A192, <http://dx.doi.org/10.1137/130924408>.
- [26] Charbel Farhat, Philip Avery, Todd Chapman, Julien Cortial, Dimensional reduction of nonlinear finite element dynamic models with finite rotations and energy-based mesh sampling and weighting for computational efficiency, *Int. J. Numer. Methods Eng.* 98 (9) (2014) 625–662, <http://dx.doi.org/10.1002/nme.4668>.
- [27] Todd Chapman, Philip Avery, Pat Collins, Charbel Farhat, Accelerated mesh sampling for the hyper reduction of nonlinear computational models, *Int. J. Numer. Methods Eng.* 109 (12) (2017) 1623–1654, <http://dx.doi.org/10.1002/nme.5332>.
- [28] Bradley Efron, Trevor Hastie, Iain Johnstone, Robert Tibshirani, Least angle regression, *Ann. Stat.* 32 (2) (2004) <http://dx.doi.org/10.1214/009053604000000067>.
- [29] Joachim Schöberl, Sabine Zaglmayr, High order nédélec elements with local complete sequence properties, 24 (2) (2005) 374–384, <http://dx.doi.org/10.1108/03321640510586015>.
- [30] Joachim Schoeberl, C++11 Implementation of Finite Elements in NGSolve, 2014.
- [31] Joachim Schöberl, NETGEN An advancing front 2D/3D-mesh generator based on abstract rules, *Comput. Vis. Sci.* 1 (1) (1997) 41–52, <http://dx.doi.org/10.1007/s007910050004>.